J. Fluid Mech. (2009), *vol.* 632, *pp.* 227–243.
doi:10.1017/S0022112009006491 Printed in the United Kingdom

Thermally driven exchange flow between open water and an aquatic canopy

XUEYAN ZHANG† AND HEIDI M. NEPF

Department of Civil and Environmental Engineering,
Massachusetts Institute of Technology,
Cambridge, MA, USA

(Received 3 September 2008 and in revised form 6 February 2009)

Differential solar heating can result from shading by rooted emergent aquatic plants, producing a temperature difference between vegetated and unvegetated regions of a surface water body. This temperature difference will promote an exchange flow between the vegetation and open water. Drag associated with the submerged portion of the plants modifies this exchange, specifically, changing the dominant velocity scale. Scaling analysis predicts several distinct flow regimes, including inertia-dominated, drag-dominated and energy-limiting regimes. After a constant heat source is initiated, the flow is initially inertial, but quickly transitions to the drag-dominated regime. The energy-limiting regime is not likely to occur in the presence of rooted vegetation. Laboratory experiments describe the exchange flow and confirm the scaling analysis. Particle Imaging Velocimetry (PIV) was used to quantify the velocity field. Once the exchange flow enters the drag-dominated regime, the intrusion velocity u_V is steady. The intrusion velocity decreases with increasing density of vegetation. The thickness of the intruding layer is set by the length scale of light penetration.

1. Introduction

Spatial heterogeneity in water temperature can generate gradients in water density, which in turn can produce convective exchange flows. In lakes, these thermally driven exchange flows play an important role in the transport of nutrients and other chemicals, and thus can have a significant effect on the lake-scale chemistry and ecology (James & Barko 1991; MacIntyre & Melack 1995). Temperature differences can occur between the shallow and deep regions of a water body. During the daytime, uniform solar radiation causes the temperature within the shallow region to rise more rapidly than that in the adjacent deeper region, because the same heat flux is distributed over a smaller water depth. Similarly, during the night, as the heat leaves the water, the temperature in the shallow region drops more rapidly than that in the deeper region. This diurnal cycle of temperature difference has been observed to generate diurnally varying exchange flows between the littoral zone and the main body of a lake (Adams & Wells 1984; Monismith, Imberger & Morison 1990; James, Barko & Eakin 1994). Under weak wind conditions, this exchange flow controls the flushing of the littoral zone, reducing the flushing time by several orders of magnitude from turbulent diffusion alone. The exchange flow generated by the differential heating and cooling associated with depth variation has also been studied through laboratory

† Email address for correspondence: xyzhang@mit.edu

experiment (Sturman & Ivey 1998; Sturman, Oldham & Ivey 1999; Lei & Patterson 2002*a*) and modelling (Horsch & Stefan 1988; Farrow & Patterson 1993; Lei & Patterson 2002*b*; Farrow 2004). In most of these studies, the variation in depth is modelled as a triangular wedge. These studies provide a clear understanding of the transient and steady components of depth-driven thermal exchange flow, as well as the pattern of reversing flow that is generated by the diurnal cycle of heating and cooling.

Exchange flow due to differential internal heating was first studied by Patterson (1984), who provided the basic scaling analysis for unsteady natural convection due to an internal heat source that was constant vertically and in time, but varied longitudinally. Trevisan & Bejan (1986) studied a similar problem, but modelled the internal heat source as that generated by the absorption of solar radiation through the surface. Following this, Coates & Patterson (1993) experimentally studied the unsteady convection produced when part of a water surface is heated, and part is shaded by an opaque layer. Initially, the exchange flow was controlled by the balance between acceleration and the buoyancy-induced pressure gradient. The intrusion velocity in this regime increased with time as $t^{3/2}$. Following this, the thermally driven exchange flow was controlled by inertia, during which time its velocity varied as $t^{1/2}$. Eventually, the exchange velocity became constant in an energy-limiting regime, in which the rate of absorption of energy is balanced by the rate of energy removal through advection.

Shading by vegetation can also cause differential heating (Ultsch 1973; Chimney, Wenkert & Pietro 2006). For example, dense vegetative stands can reduce incident light by 50 % to over 90 % (Wetzel 2001). Pokorný & Květ (2004) observed the water temperature in a stand of *Nuphar lutea* to be as much as 4°C lower than the surrounding open water during daytime. Similarly, Lightbody, Avener & Nepf (2008) reported that the daytime temperature within the marsh region of a constructed wetland remained 2°C cooler than the adjacent open water areas. Coates & Ferris (1994) showed that shading from floating plants can generate an exchange flow. However, the flow was displaced downward, beneath the root layer. As an extension to Coates & Ferris (1994), this paper will examine the impact of rooted vegetation, for which the root obstruction extends over the entire depth.

Rooted vegetation provides a significant amount of drag, such that we expect rooted plants to both promote, through differential shading, and inhibit, through drag, the thermally driven exchange flow. Tanino, Nepf & Kulis (2004) studied the impact of canopy drag on exchange flows by generating a lock exchange within an array of circular cylinders that extended through the entire water depth. They identified distinct flow structure for the two different drag regimes, namely, linear and quadratic drag. In addition, the drag associated with the array significantly reduced the exchange velocity, compared with the classic unobstructed exchange flow. Zhang & Nepf (2008) considered the more natural case of exchange between a model canopy and an adjacent region of unobstructed water. The velocity of the intrusion entering the canopy as well as the total discharge between the open water and the canopy were strongly dependent on the canopy drag. Tanino *et al.* (2004) and Zhang & Nepf (2008) considered cases in which the reduced gravity g' was constant, set by the density difference between the initial reservoirs. In this work, g' is not constant because it is generated by spatial variation in a steady heat source, mimicking the evolution of shaded and unshaded regions receiving uniform solar radiation. Under a constant heat source, the temperature difference between the shaded and unshaded regions ΔT increases linearly with time, such that g' also increases linearly with time.

The importance of both differential heating and of aquatic vegetation to the ecology and water quality of lakes and reservoirs is well recognized. However, most previous studies have been limited to either exchange flow due to differential heating/cooling or due to the effects of vegetation. Oldham & Sturman (2001) examined the impact of vegetative drag on the convective flushing of the littoral zone, associated with depth-differential-cooling. However, the combined effects of vegetative shading and vegetative drag on an exchange flow have not received specific attention. This is the focus of the current study. Compared to (Coates & Patterson 1993; Coates & Ferris 1994) classic studies of differential shading, the current work adds the impact of rooted vegetation, providing new insight to a wider range of natural conditions.

2. Model development and scaling analysis

When solar radiation impinges on a water surface, a significant portion is reflected from the surface and is lost through scattering. The remaining energy penetrates the surface and is absorbed by the water. Due to absorption, the light intensity or irradiance I decreases with distance from the water surface following Beer's Law,

$$I(z) = \sum_{i=1}^{n} I_i \exp\left[-\eta_i(h-z)\right]. \tag{1}$$

Here, I_i and η_i are the radiation intensity and the extinction coefficient associated with a particular wavelength, h is the total water depth and z is the height measured from the bed and is positive upward. The extinction coefficient η_i an increases with on turbidity. The infrared band of the spectrum is most easily absorbed in water, and most of the energy associated with the infrared region is absorbed near the water surface. The absorption of light decreases with decreasing wavelength and reaches a minimum absorption for blue, and then increases again in the ultraviolet (UV) region. According to Wetzel (2001), about 53 % of the total light energy is transformed into heat and absorbed in the first metre of water. For the purpose of parameterization and application in the field, we consider the bulk behaviour of the incoming light and adopt a single-band model, i.e. a single value of I_0 and η to represent the behaviour of the full spectrum of light, in which I_0 is the total energy input at the surface and η is the bulk extinction coefficient, representing a composite for all wavelengths (Coates & Ferris 1994; Lei & Patterson 2002*a*). Beer's Law can then be written as

$$I(z) = I_0 \exp\left[-\eta(h-z)\right]. \tag{2}$$

Now, consider a rectangular domain of constant depth h and total length $(L_V + L_O)$, in which L_V and L_O are the lengths of the vegetated and open region, respectively (figure 1). In this work, we assume that the emergent portions of the rooted plants completely block the incoming solar radiation. Under constant heat flux I_0, the water in the open region heats up, and becomes less dense than the adjacent water in the vegetation. This density difference drives an intrusion of warm water into the vegetated region at the surface, with a compensating return flow underneath. The intrusion depth h_I is expected to scale with $1/\eta$, which according to Beer's Law (2) is the length scale of heat absorption. In some cases this length scale might be modified by thermal diffusion. However, the diffusion length scale, $\sqrt{\kappa t}$, with κ the thermal diffusivity of water, grows too slowly to impact the exchange flow considered here. Specifically, in 1 h, diffusion could deepen the heated layer by only 1 cm.

In the field, the extinction coefficient varies from 0.1 to 10 m^{-1}, so that we expect that h_I ranges from $O(10)$ cm to $O(10)$ m. As shown in figure 1, when $h_I < h/2$, the

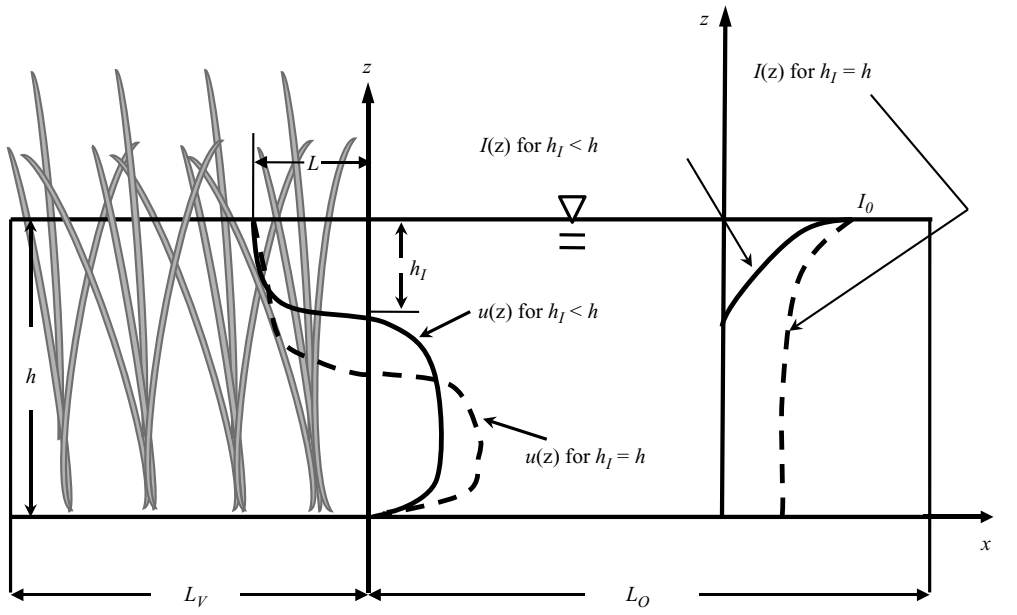

FIGURE 1. A sketch of thermal and intrusion length scales.

extinction coefficient should set the depth of the intrusion layer, $h_I \sim 1/\eta$. However, the total water depth likely constrains the intrusion depth for $h_I > h/2$.

In the littoral regions of a lake, the horizontal length scale is generally much greater than the water depth. The viscous term $\nu(\partial^2 u/\partial x^2)$ is thus much smaller than $\nu(\partial^2 u/\partial z^2)$ and can be neglected. The conservation of horizontal momentum in a two-dimensional system is then

$$\frac{\mathrm{D}u}{\mathrm{D}t} = -\frac{1}{\rho}\frac{\partial P}{\partial x} - Cau + \nu\frac{\partial^2 u}{\partial z^2}, \tag{3}$$

where u is the horizontal velocity component, P is the pressure, ρ is the fluid density, ν is the kinematic viscosity of water and x and z are horizontal and vertical axes, respectively and t is time. The second term on the right-hand side characterizes the vegetative drag, and a is the frontal area of vegetation per unit volume. C ($\mathrm{m\,s^{-1}}$) is a linear drag coefficient. A linear drag law is selected based on the expected range of stem Reynolds number. Based on Coates & Patterson (1993), the velocity of an exchange flow produced by surface shading without vegetation can be of the order of $0.1\ \mathrm{cm\,s^{-1}}$. This value can be regarded as an upper limit for the cases being considered here, which will be damped by vegetative drag. Typical values of stem diameter for aquatic plants are between 0.5 and 1 cm, indicating a typical stem Reynolds number ($Re_d = ud/\nu$) of less than 10. Previous studies by Tanino *et al.* (2004) and Zhang & Nepf (2008) have shown that a linear drag law is appropriate in characterizing the flow at this range of Reynolds number. As we will show later, the Reynolds numbers for our experiments range from 0.8 to 3. In addition, we will consider model vegetation with densities between solid volume fraction 3 % and 15 %. Koch & Ladd (1997) modelled the drag produced by random arrays of cylinders with solid volume fraction between 5 % and 40 % and Reynolds number between 0.2 and 180. In this work, we will estimate the drag coefficient C based on drag values reported in Koch & Ladd (1997).

The following scaling is introduced:

$$x \sim L, \quad z \sim h_I, \quad \Delta P \sim \Delta\rho g h_I \sim \rho\alpha\Delta T g h_I, \tag{4}$$

in which L is the horizontal length scale of the intrusion in the canopy (figure 1). $\Delta\rho$ is the density difference between the canopy and open water and ΔP is the resulting pressure difference. α is the coefficient of thermal expansion. g is gravity. The temperature difference ΔT increases with time due to the constant heat flux I_0 impacting the water in the open region only. The temperature difference can be expressed as $\Delta T = I_0 t/\rho C_P h_I$, where C_P is the specific heat of water. With the above scaling (3) can be written in the following form:

$$u^2 \sim -\frac{g\alpha I_0 t}{\rho C_P} - CauL + \nu\frac{uL}{{h_I}^2}. \tag{5}$$

We assume that the system starts from rest with $L = 0$. Therefore, in the initial period after the heat flux has started, the system is controlled by the balance between inertia and buoyancy only, i.e. the last two terms in (5) drop out for small L. Equating the first and second terms in (5), the velocity scale for the inertia-dominated regime, u_i, can be found.

$$u_i \sim \left(\frac{g\alpha I_0 t}{\rho C_P}\right)^{1/2} \sim \sqrt{g' h_I}, \tag{6}$$

where g' is obtained by

$$g' = \frac{\Delta\rho}{\rho} g = \alpha\Delta T g = \frac{g\alpha I_0 t}{\rho C_P h_I}. \tag{7}$$

The result given by (6) is mathematically similar to the theory for the classic gravity current, except that the reduced gravity g' is not constant, but increases linearly with time, resulting in $u_i \sim t^{1/2}$. The same scaling was previously derived by Coates & Patterson (1993) for flows in the absence of rooted vegetation. Coates & Patterson (1993) also noted that prior to the inertia-dominated regime, the conduction length scale, $\sqrt{\kappa t}$, is briefly dominant and the velocity scale in this regime varies with $t^{3/2}$. However, this regime is very short-lived and is not considered here.

As the intruding front lengthens ($L > 0$) over time, both the viscous and vegetative drag become important. For most canopies the vegetative drag will dominate, as is shown by comparing the two drag terms. Specifically, vegetative drag will dominate when

$$\frac{Cah_I^2}{\nu} \gg 1. \tag{8}$$

In typical aquatic systems, $a = O(0.01\text{–}0.1\ \mathrm{cm}^{-1})$, which corresponds to roughly 100–1000 stems m^{-2} (Kadlec 1990). With $Re_d = O(100)$ and $C \approx 1\ \mathrm{cm\,s}^{-1}$ (Tanino *et al.* 2004) (8) shows that viscous drag can be neglected for $h_I \gg 0.3$ cm. This condition will generally be met in the field, as well as in our laboratory studies. While evaluating (8), we assumed the flow to be laminar, i.e. we consider molecular viscosity ν. This can be justified by considering $h_I = O(10\ \mathrm{cm})$ and $u \leqslant 0.1\ (\mathrm{cm\,s}^{-1})$ (Coates & Patterson 1993), $Re_{h_I} = uh_I/\nu \leqslant O(100)$. Therefore, we anticipate that the laminar flow assumption will be correct for most conditions.

By comparing the terms for vegetative drag and inertia in (5), we anticipate that vegetative drag will dominate when $u \ll CaL$. Recognizing $L = ut$, the time scale at which vegetative drag will exceed inertia is

$$T_V \sim (Ca)^{-1}. \tag{9}$$

With the values for a and C given above, T_V is estimated to be O(10–100 s), which indicates a short duration of inertial flow, e.g. as compared to the time scale of daily heating O(12) h. After this time, the velocity is determined by the balance of buoyancy and vegetative drag. Equating these terms in (5), and using $L = ut$, gives

$$u_V \sim \left(\frac{g\alpha I_0}{\rho C_P C a}\right)^{1/2}. \tag{10}$$

It is interesting to see that the velocity is steady in this regime. Although the buoyancy increases with time due to the constant heat flux, $g' = \alpha g I_0 t/\rho C_P h_I$, the vegetative drag on increases with increasing intrusion length, $L \sim t$, and the two affect balance.

Previous studies considered the case with a constant buoyancy (e.g. ΔT, $\Delta\rho$ being fixed, such that g' is fixed), for which (10) reduces to

$$u_{Vg'} \sim \left(\frac{g' h_I}{Cat}\right)^{1/2}. \tag{11}$$

The subscript g' denotes constant g' condition. For constant g', the velocity decreases with time. This scaling was verified by Tanino *et al.* (2004) and Zhang & Nepf (2008) for the case $h_I = h$. Finally, since we anticipate that the extinction coefficient η sets the depth of intrusion h_I, it is reasonable to write the volume discharge rate under constant flux I_0 as

$$q \sim \left(\frac{g\alpha I_0}{\rho C_P C a}\right)^{1/2} \frac{1}{\eta}. \tag{12}$$

The energy balance provides another possible control on the velocity, because the flow cannot carry away more heat than is supplied by the surface flux (Coates & Patterson 1993). In the energy-limiting regime, the surface flux per unit width, $I_0 L_O$, is balanced by the advective flux per unit width, i.e.

$$I_0 L_O = u\rho C_P \Delta T h_I. \tag{13}$$

Recall that L_O is the length of heated surface in the open water region (figure 1). From (13), the energy-limiting velocity scale is found to be (as in Coates & Patterson 1993)

$$u_E \sim \frac{I_0 L_O}{\rho C_P \Delta T h_I}. \tag{14}$$

Once the flow has reached the energy-limiting regime, the heat fluxes are in balance and ΔT will be constant. The value of ΔT in this regime depends on how long it takes to reach the energy-limiting regime, which in turn depends on whether the drag-dominated regime is reached before or after the energy-limiting regime. First, consider the case in which the flow is inertia dominated until reaching the energy-limiting regime. Equating the inertial velocity scale u_i in (6) to the energy-limiting velocity scale in (14), and using $\Delta T = I_0 t/\rho C_P h_I$, the time scale to reach the energy-limiting regime is given by

$$T_E \sim \left(\frac{\rho C_P {L_O}^2}{g\alpha I_0}\right)^{1/3}. \tag{15}$$

This result was previously derived by Coates & Patterson (1993) for differential heating without vegetation. With typical field values of $I_0 = 515$ W m^{-2} and $L_O = 100$ m (as suggested by Coates & Patterson 1993) (15) gives $T_E = 3500$ s, which is much longer than the time required for the vegetative drag to dominate, $T_V = 10$–100 s.

Case	ϕ	a (m^{-1})	h ($\pm$0.1)cm	I_0 ($W\,m^{-2}$)	η (m^{-1})	C ($m\,s^{-1}$)
1	0.03	6.37	10.0	157 ± 1	6.65 ± 0.04	0.0046
2	0.05	10.6	10.0	157 ± 1	6.65 ± 0.04	0.0051
3	0.08	17.0	10.0	157 ± 1	6.65 ± 0.04	0.0058
4	0.12	25.5	10.0	157 ± 1	6.65 ± 0.04	0.0074
5	0.15	31.9	10.0	157 ± 1	6.65 ± 0.04	0.0091
6	0.03	6.37	15.0	157 ± 1	6.65 ± 0.04	0.0045
7	0.05	10.6	15.0	157 ± 1	6.65 ± 0.04	0.0048
8	0.08	17.0	15.0	157 ± 1	6.65 ± 0.04	0.0056
9	0.12	25.5	15.0	157 ± 1	6.65 ± 0.04	0.0073
10	0.15	31.9	15.0	157 ± 1	6.65 ± 0.04	0.0091
11	0.03	6.37	10.0	183 ± 1	5.98 ± 0.02	0.0045
12	0.05	10.6	10.0	183 ± 1	5.98 ± 0.02	0.0051
13	0.08	17.0	20.0	183 ± 1	5.98 ± 0.02	0.0057
14	0.12	25.5	15.0	200 ± 2	7.02 ± 0.03	0.0074
15	0.05	10.5	15.0	200 ± 2	7.02 ± 0.03	0.0049
16	0.08	17.0	15.0	200 ± 2	7.02 ± 0.03	0.0057

TABLE 1. Summary of experimental conditions and model parameters.

Therefore, under typical conditions, the drag-dominated regime will occur first, and once achieved it will set up a steady flow, i.e. u_V is constant and ΔT increases over time. This is different from the result of Coates & Patterson (1993) in which the inertia-dominated regime is followed by the energy-limiting regime. That is, the contribution of vegetation drag changes the dominant velocity scale.

Since the vegetative drag becomes important at very early time, we now revise our estimate for the time scale at which the energy-limiting regime is reached. By equating the drag-dominated velocity u_V given in (10) to u_E given in (14), along with $\Delta T \sim (I_0 t/\rho C_p h_1)$, we have

$$T_E \sim \left(\frac{\rho C_P C a {L_O}^2}{g\alpha I_0}\right)^{1/2}. \tag{16}$$

Using the representative values given above, $T_E = 6.5 \times 10^4$ s, or roughly 18 h. Given the diurnal heating cycle is typically 12 h or less, this time scale indicates that under typical field conditions the energy-limiting regime is unlikely to occur, and the exchange flow is completely controlled by the drag-dominated regime.

3. Experimental procedures

To test the above scaling analysis, a series of experiments was conducted in a Plexiglas® tank with dimensions of $70\,(L) \times 15\,(W) \times 40\,(H)$cm. The tank consisted of two separate chambers, shown in figure 2. Two 600 W spotlights were used to produce a uniform heat source. Different combinations of the two spotlights produced three different radiation intensities (table 1). A mirror was mounted over the tank to direct the parallel light from the spotlights vertically downward into the experimental chamber. The angle of the mirror was adjusted to ensure a sharp edge between the open region and the shaded region. The aperture of the spotlight was wider than the tank, so that only the central region of the light was used for heating. This ensured that the incoming light uniformly illuminated the open water.

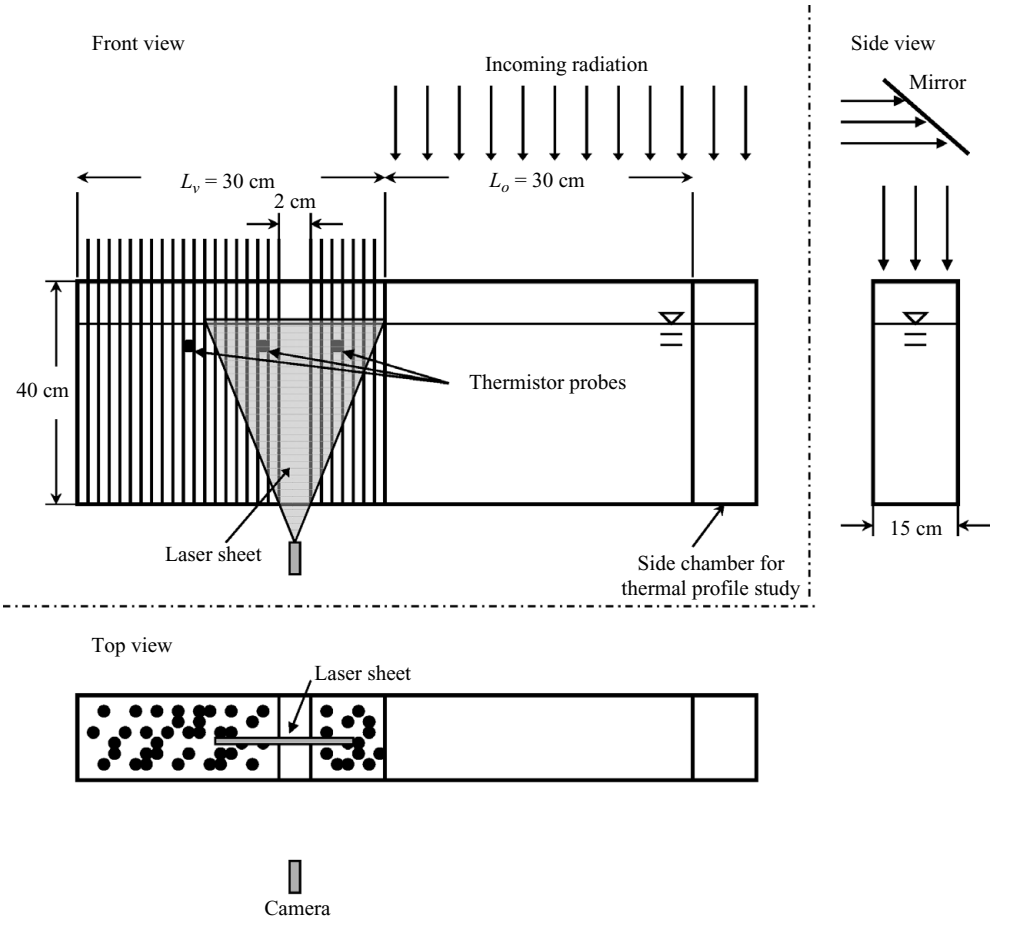

FIGURE 2. A sketch of the experimental setup. The sketch is not plotted to scale. Specifically, the width of gap for PIV is the same order of magnitude or smaller than the distance between dowels.

Temperature measurements were made using four submersible Hart Scientific® 5611-T teflon thermistor probes. The probe tip was 3 mm in diameter and the sensor was 13 mm long. The thermistor probe had a measuring range of 0°C–100°C with an accuracy of 0.0025°C. A 1529 Chub-E4 Thermometer was used to simultaneously log temperature data from the four probes at a sampling rate of 1 Hz.

On one side of the tank, a side chamber with dimensions of $10\,(L) \times 15\,(W) \times 40\,(H)$ cm was separated from the main chamber. This region was used to determine the values of I_0 and η. Because of the narrowness of the side chamber, fluid motions were prohibited. If we neglect conductive heat transfer within the water, the temperature change at depth z can be expressed as

$$T(z,t) = \frac{I_0\eta}{\rho C_p}\,\exp[-\eta(h-z)]t. \tag{17}$$

Differentiating (17) with time gives the time rate of change of temperature,

$$\frac{\partial T(z,t)}{\partial t} = \frac{I_0\eta}{\rho C_p}\,\exp[-\eta(h-z)]. \tag{18}$$

Under a constant heat source, i.e. I_0 constant, temperature increases linearly over time, and $\partial T(z,t)/\partial t$ is constant. Using temperature data from two different depths, e.g. $T(z_a,t)$ and $T(z_b,t)$, we can use (18) to find the following relation:

$$\frac{\partial T(z_a,t)/\partial t}{\partial T(z_b,t)/\partial t} = \exp[-\eta(z_b - z_a)]. \tag{19}$$

Temperature records and (19) were used to find the extinction coefficient η. The radiation intensity I_0 was then found by fitting the measured temperature to (18). For this analysis, the four temperature probes were placed in the side chamber, at $z = 2$, 10, 18 and 25 cm above the bottom of the tank.

The thermally driven flow was generated in a subchamber with dimensions of $60\,(L) \times 15\,(W) \times 40\,(H)$cm, half of which was covered by a board, perforated with 6 mm holes. Cylindrical dowels with diameter $d = 6$ mm and 50 cm length were passed through randomly selected holes and extended down to the bottom of the chamber. The cylinder array was then covered by a piece of black cloth to prevent light from going through unfilled holes.

The solid volume fraction ϕ ranged from 3 % to 15 %, corresponding to a frontal area per unit volume of $a = 0.01$–0.05 cm^{-1}. In the field, solid volume fraction varies from a lower limit of $\phi = 1$ % (water lily) to an upper limit of $\phi = 40$ % (mangroves). Because of the difficulty in visualizing flow within a dense dowel array, our work was restricted to cases up to $\phi = 15$ %. To track the intrusion, three thermistor probes were placed within the model canopy along the centreline of the tank and, at distances of 6.5, 13.0 and 19.5 cm from the canopy edge, and at 2 cm below the water surface. This depth was chosen to fall in the middle of the intruding layer, based on preliminary observations. Stainless steel rods of the same diameter as the dowels were used to hold the probes. To position the probes, small holes were drilled in the rods 1 cm apart, with an accuracy of ± 1 mm. After the light was turned on, the thermometers logged temperature for the duration of the experiment at a frequency of 1 Hz. For some experiments, an additional temperature probe was placed at 13.0 cm, but located near the sidewall of the tank. Comparing the two probes located at the same longitudinal (13 cm) but different transverse positions confirmed that there were no preferential flow paths, and the intrusion was approximately uniform over the tank width.

Particle imaging velocimetry (PIV) was used to quantify the flow field within the model vegetation. Pliolite® particles with a density of 1.02 g cm^{-3} were added to the water. A 2 cm wide gap starting at 8 cm from the edge of the canopy was left within the model canopy as a window for the PIV. The width of the gap was chosen to be the same order of magnitude as or smaller than the distance between dowels. A laser sheet entering through the bottom of the tank illuminated the gap. The laser power was kept low enough (0.3 W) to prevent thermal plumes from being generated due to the heating of the bottom wall of tank. Preliminary experiments also confirmed that no thermal plumes were formed on the sidewalls due to heating by the spot light.

Coates & Patterson (1993) reported in their study of exchange flow, without vegetation, that the exchange velocity generated by similar differential heating was approximately 0.1 cm s^{-1}. This can be regarded as an upper limit of the expected magnitude of flow in the present study. To improve the accuracy of PIV at such low velocity, a digital single-lens-reflex (SLR) camera with a maximum resolution of 3872×2592 pixels was used to capture the flow field at a frame rate of 0.5 fps. Given the resolution of the camera, 1 pixel was approximately equal to a distance of 0.005 cm. Consequently, the PIV technique could resolve velocities of the order of 0.005 cm s^{-1}. The image acquisition was started after the intrusion had passed the

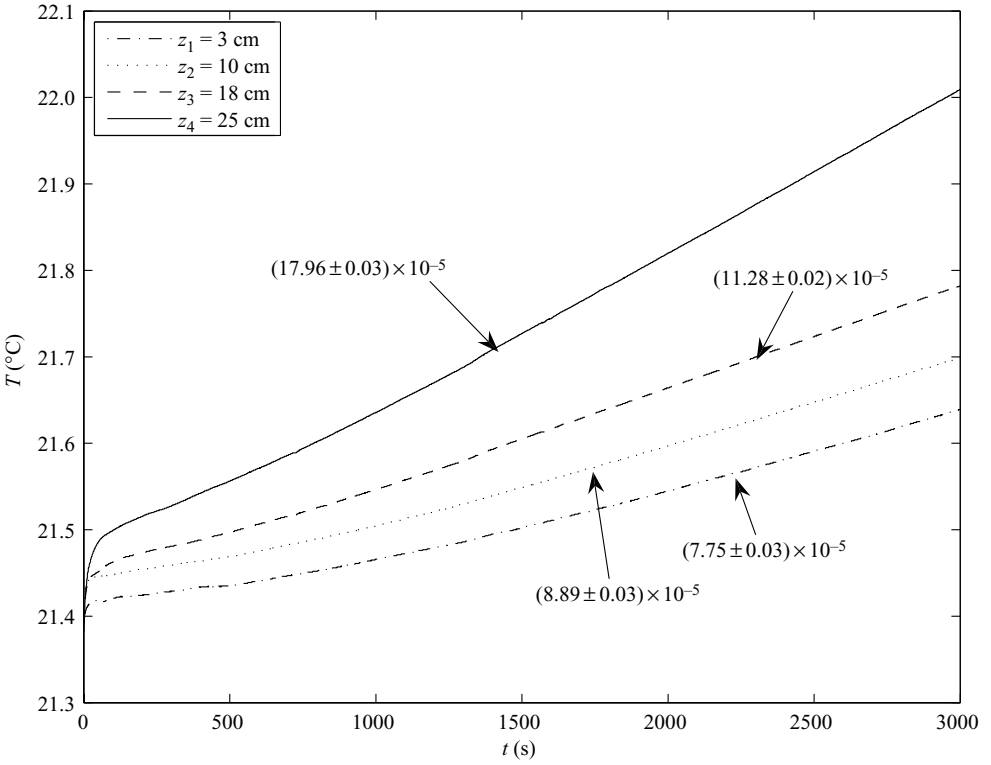

FIGURE 3. The time variation of temperature at different depths under constant heat source. Numbers are the average time rate of change of temperature at each depth ($^{\circ}\mathrm{C\,s^{-1}}$). The temperature data was collected in the side chamber.

PIV window located at 8 cm. The passage of the intrusion front was indicated by an increase in the temperature at the 13 cm thermistor. Fifty pictures were taken for each experiment. MatPIV v. 1.6.1, a Matlab software package, was used to calculate the velocity field from the pictures. Details about the PIV technique can be found in Gharib & Daribi (2000) and Sveen (2004).

After the velocity field was obtained from PIV, a velocity profile was extracted from the middle of the PIV window. The velocity profiles within each 10 s interval, i.e. five pictures, were averaged to remove noise. The averaged velocity profiles were integrated over depth to confirm conservation of volume, i.e. the volume of the intruding layer was equal to that of the outflow. The depth of intrusion h_I was defined by the position at which the velocity component changed its direction from inflow to outflow. The mean intrusion velocity U_{mean} was calculated by averaging the velocity profile from the surface to the depth of the intrusion.

4. Results

For each radiation intensity we evaluated I_0 and η using the narrow side chamber. Under constant heat flux I_0 the temperature increased linearly with time, as expected (figure 3). The time rate of change of temperature was larger near the surface than at depth, indicating that more energy is absorbed near the water surface, which agrees with previous observations (Wetzel 2001). The pair of sensors nearest the surface

($z_3 = 18$ cm and $z_4 = 25$ cm) were used to calculate I_0 and η. The radiation intensity and the extinction coefficient for all cases are summarized in table 1.

In our model the extinction coefficient was between 6 and $7\,\mathrm{m}^{-1}$, consistent with previous similar models used by Coates & Patterson (1993) and Lei & Patterson (2002*a*), who reported values of 21.6 and $6.2\,\mathrm{m}^{-1}$, respectively, for clear water in laboratory tank. In contrast, the extinction coefficients found in natural lakes range from $\eta = 0.2\,\mathrm{m}^{-1}$ in very clear lakes to $4\,\mathrm{m}^{-1}$ in lakes with typically high turbidity (Wetzel 2001). However, values as high as $10\,\mathrm{m}^{-1}$ have been observed in the field. Compared to the typical values observed in the field, laboratory experiments tend to report higher values for η. There are two reasons for this difference. First, in the field, η is a composite of wavelengths, ranging from infrared to ultraviolet. In the laboratory, however, the heat source is usually a stage light, whose irradiance is mainly composed of long-wave radiation, e.g. infrared to red. Since the short-wave portion penetrates more deeply into the water, excluding the short-waves results in a higher extinction coefficient. Second, in the field the calculation of the vertical extinction coefficient generally excludes data from the first metre below the surface because of surface agitation (Wetzel 2001), and this excludes some fraction of the long-wave radiation, artificially reducing η.

After the spotlight was turned on, a temperature difference between the illuminated and shaded regions appeared and grew with time. An intrusion of warmer water entered the model canopy. Temperature probes positioned in the canopy marked the arrival of this intrusion. The temperature change δT with respect to the initial temperature at each location is shown in figure 4. Initially, $\delta T = 0$, indicating that the warm intrusion has not yet reached a given location. The rise in temperature marks the arrival of the intrusion, and the subsequent steady linear increase of temperature is consistent with an intrusion of constant velocity. For example, the temperature at $x = -6.5$ cm started to rise at $t = 300$ s, and the temperature at $x = -13.0$ cm started to rise at $t = 500$ s (figure 4). The temperature data at $x = -6.5$ cm and $x = -13.0$ cm exhibit a small drop in temperature, just preceding the steady increase. This is attributed to a downward vertical motion that precedes the intrusion front. Before starting the experiments, the tank sat in the laboratory for several hours to equilibrate with the room. During this period, the surface temperature became slightly lowered, due to surface heat loss. According to previous laboratory observations (Zhang & Nepf 2008) and numerical studies (Jamali, Zhang & Nepf 2008), downward motion is induced just ahead of the intruding front. We believe this localized downward motion delivers cooler surface water past the probe just before the intrusion arrives, creating a short drop in temperature preceding the steady rise in temperature that marks the passage of the intrusion. It was also observed that the temperature at $x = -19.5$ cm increased mildly starting at about 300 s and then increased sharply after the warm intruding current passed this position. We believe that the mild increase in the temperature in the thermistor located at -19.5 cm is due to the laser light sheet used for PIV. We turned the laser on when we observed the first temperature probe started to rise. It is possible that the outer edge of the laser sheet heated the water near the far thermistor, and caused the mild increase of the temperature before the arrival of the intrusion. In subsequent studies, we shuttered the laser to reduce this effect.

PIV measurements confirmed that after the intrusion has passed the PIV window, the velocity was predominantly horizontal. The predominantly horizontal flow is consistent with previous experimental observations by Coates & Patterson (1993) and Coates & Ferris (1994) for thermally driven flow, and Zhang & Nepf (2008) for lock-exchange flow. A vertical profile of velocity was extracted from the centre of

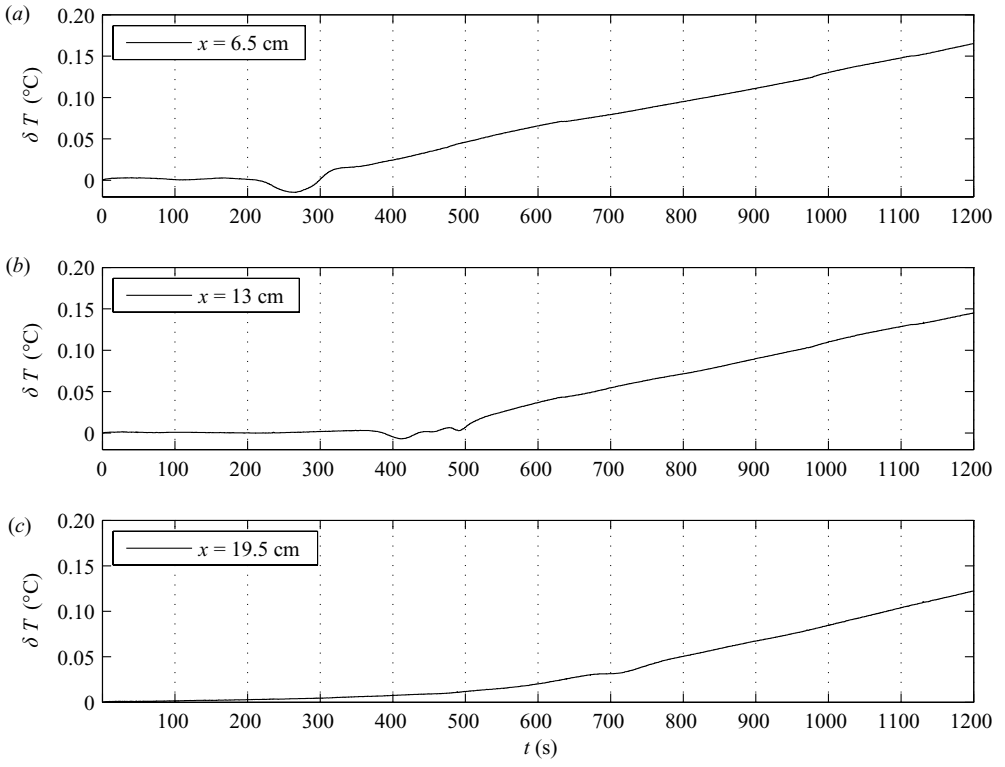

FIGURE 4. Temperature change of water in the shaded region for case 1, after the start of experiment, at (*a*) $x = -6.5$ cm, (*b*) $x = -13.0$ cm, (*c*) $x = -19.5$ cm. δT is the temperature change with respect to its initial temperature.

the PIV window. Two examples for $a = 6.4$ m^{-1} are shown in figure 5. The velocity profiles maintained the same shape and magnitude over the duration of the PIV measurements (100 s), in agreement with our scaling analysis, which predicts a steady intrusion velocity for the drag-dominated regime, as shown in (10). For the cases shown in figure 5, the flow transitions to the drag-dominated regime at $T_V = 30$ s based on (9). Therefore, the velocity profiles shown in figure 5 were in the drag-dominated regime. Note that, it was also observed that the intrusion consists of a single layer, despite the fact that the layer is vertically stratified. A single-layer intrusion was also observed by Coates & Patterson (1993). These observations indicate that the vertical stratification within the layer was not dynamically important. In each case the maximum intrusion velocity was 0.09 cm s^{-1}. The return flow, however, decreased with increasing total water depth, i.e. compare figure 5(*a*) ($h = 10$ cm) and figure 5(*b*) ($h = 15$ cm). This is consistent with continuity. Indeed, as the total water depth approaches infinity, the return flow would become vanishingly small. Finally, the parabolic shape of the velocity profile near the bed indicates the development of a viscous boundary layer (figure 5).

The intrusion depth h_I was extracted from each velocity profile, and the variability within each experimental run used as an estimate of uncertainty. The normalized intrusion depth ηh_I for each run is shown in figure 6. There is no systematic correlation between the normalized intrusion depth ηh_I and ah, implying that the surface intrusion depth is not controlled either by the total water depth h or the

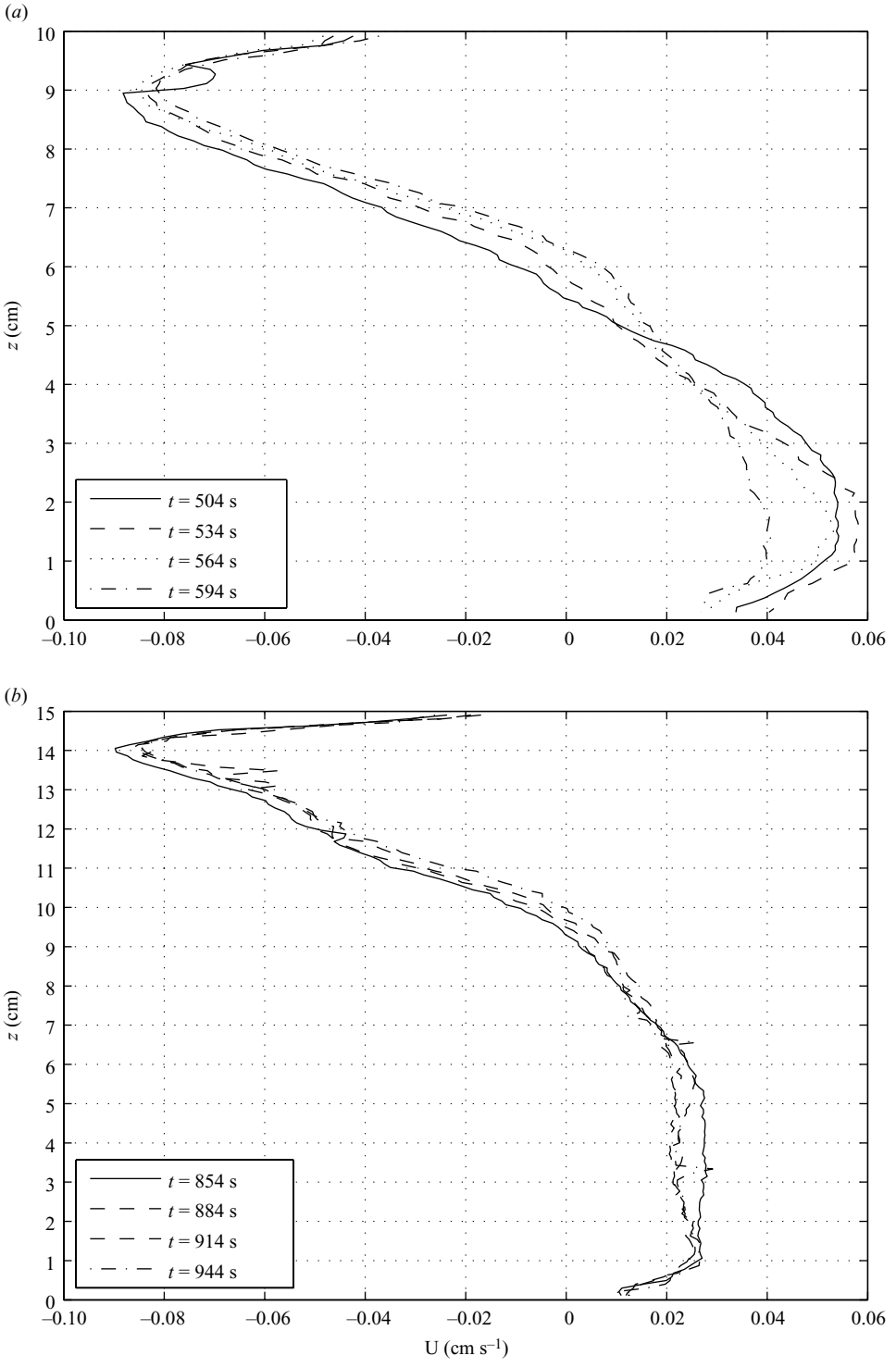

FIGURE 5. Profiles of horizontal velocity sampled at 9 cm from the edge of the canopy, for $h = 10$ cm and $a = 6.37\,\mathrm{m}^{-1}$ (case 1 (*a*)) and $h = 15$ cm and $a = 6.37\,\mathrm{m}^{-1}$ (case 6 (*b*)). Note that the z-axes are not the same scale.

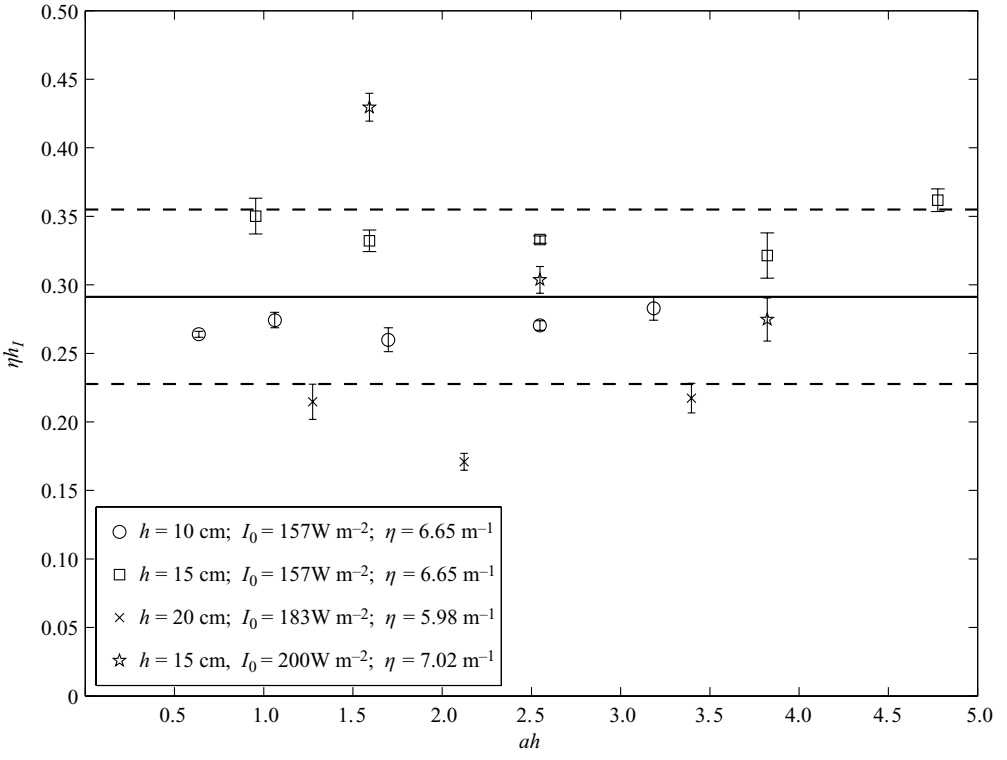

FIGURE 6. Variation of the normalized intrusion depth ηh_I with ah. The error bars show the standard error for each run. The solid line is the average of ηh_I for all cases. The dashed lines are one standard deviation from the average.

canopy density a. Using all available runs, $\eta h_I = 0.28 \pm 0.06$, which is shown by the solid line in figure 6. For similar heating conditions, Coates & Patterson (1993) found $\eta h_I = 0.65$.

Profiles of velocity, as shown in figure 5, were used to estimate the mean intrusion velocity U_V. A second estimate of U_V can be made from the temperature records, such as those shown in figure 4. Specifically, we divided the distance between two temperature probes by the time interval between the arrivals of the intrusion, as indicated by the onset of the steady increase of temperature. For every run the velocities calculated from PIV and from the temperature records were the same within uncertainty (data not shown). This confirms that the velocity measured at the PIV window is representative of the velocity at the intrusion front, i.e. the velocity is constant along the length of the intrusion.

For comparison, the drag-dominated velocity u_V given in (10) is normalized by the viscous-dominated velocity scale, which was derived in Coates & Patterson (1993). This velocity ratio is proportional to the ratio of viscous stress to vegetative drag, as shown by the third term in (20),

$$u_v^* = u_V \Big/ \left[\frac{g\alpha I_0 h_I^2}{\rho C_P \nu}\right]^{1/2} \sim \left[\left(\frac{Cah_I^2}{\nu}\right)^{1/2}\right]^{-1}. \tag{20}$$

To normalize the measured velocity using (20), the linear drag coefficient C was interpolated from the numerical results of Koch & Ladd (1997), who reported drag

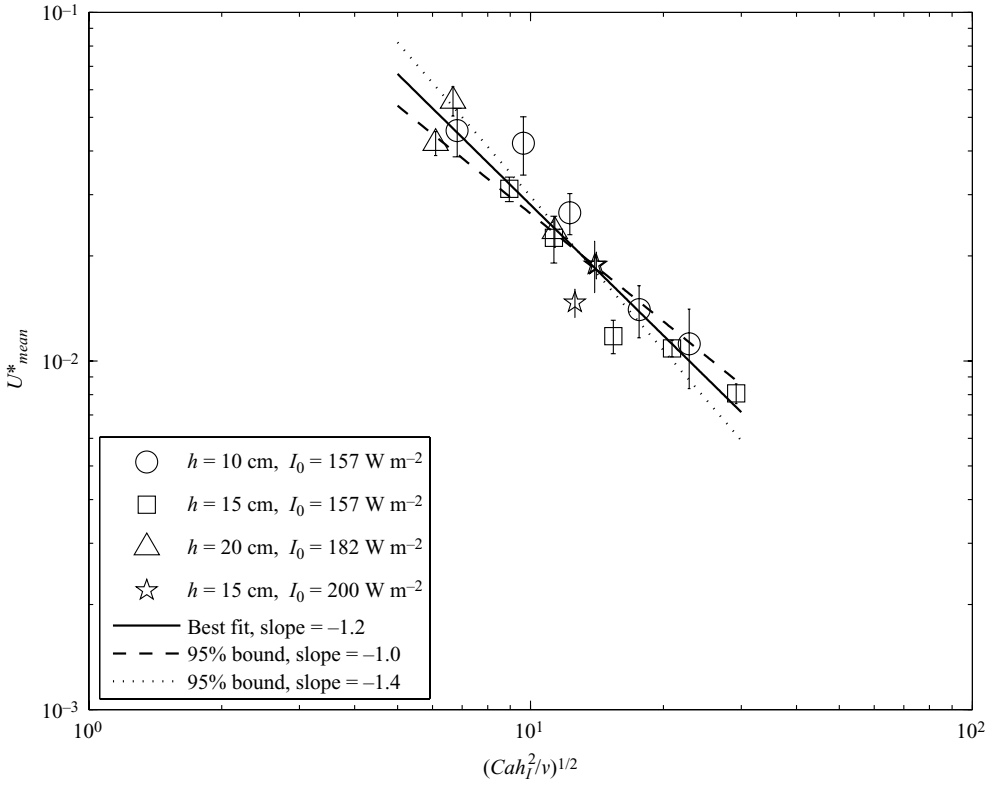

FIGURE 7. Normalized mean intrusion velocity against normalized canopy drag. The error bars show the standard error for each case. The solid line is the theoretical prediction based on (10).

for ϕ between 5 % and 40 % and Re_d between 0.2 and 180, conditions that correspond to those studied here. The estimated drag coefficients are listed in table 1. The drag coefficient is only weakly dependent on Re_d, which is consistent with our assumption of linear drag law. However, the drag coefficient increases with increasing a. As Koch & Ladd (1997) explain, as ϕ and therefore a increase, the spacing between array elements decreases, and the viscous stress, which dominates the total drag at these low Reynolds numbers, increases. Finally the average intrusion velocity U_{mean} is normalized following (20), and using the following parameters: $g = 9.8$ m s^{-2}, $\alpha = 2.1 \times 10^{-4}$ K^{-1}, $C_P = 4182$ J kg^{-1} K^{-1}, as well as the measured I_0 and η for different cases. The normalized U^*_{mean} is plotted against $(Cah_I^2/\nu)^{1/2}$ in a log–log coordinate (figure 7). The intrusion velocity decreases as the vegetative drag increases. The fitted slope, -1.2 ± 0.2 (with 95 % confidence), agrees with our theoretical prediction of -1, based on (20). We anticipate that as the vegetative drag decreases further and becomes comparable with the viscous drag, i.e. $(Cah_I^2/\nu)^{1/2} \to 1$, the normalized velocity U^*_{mean} should become $O(1)$; the intrusion velocity is then controlled by viscous drag.

5. Conclusion

This paper has examined the thermally driven exchange flow generated by the differential shading between open water and an adjacent emergent canopy under a constant light source. Scaling analyses described the expected flow regimes and

associated velocity scales. Compared to the unobstructed exchange flow studied by Coates & Patteson (1993), the presence of a rooted aquatic canopy alters the dynamics of the exchange flow; specifically, the exchange flow is controlled by vegetative drag. The drag-dominated velocity scale was confirmed by experiment. In addition, we show that the energy-limiting regime is unlikely to occur in the laboratory or in the field.

Using the typical values observed in the field, $I_0 = 515$ W m^{-2}, $L_0 = 100$ m and $\eta = 4.4$ m^{-1} (Coates & Patterson 1993), a canopy of solid volume fraction $\phi = 0.05$ will generate an average intrusion velocity of 0.06 cm s^{-1} and a mean discharge rate of 0.42 cm^3 cm^{-1}. Similarly, for a canopy of solid volume fraction $\phi = 0.15$, the average intrusion velocity will be 0.04 cm s^{-1}, with a mean discharge rate of 0.24 cm^3 cm^{-1}. The duration of the exchange flow is approximately a diurnal cycle, i.e. ~ 12 h. Over the course of 12 h, the exchange flow with $\phi = 0.15$ can flush a vegetated littoral zone of up to width $L = u_V t = 25$ m.

While our model can be used to estimate the magnitude of the exchange flow driven by thermal forcing, there are still challenges in applying our model in the field. First, the application of the model requires an input of the drag coefficient C, which is generally unknown *a priori*. Although the determination of drag coefficient has been studied in the literature, e.g. Koch & Ladd (1997) and Tanino & Nepf (2008), most work is limited to a certain range of Reynolds number, a certain range of volume fraction, or very simple morphology, i.e. circular cylinders. A universal explicit solution for C that covers a wide range of Reynolds number and solid volume fraction and vegetation morphology is still not available. Second, in most studies on vegetative drag, aquatic vegetation is modelled with a uniform morphology, such as rigid cylinders. We expect that the morphology of specific vegetation may alter the structure of the exchange flow. For example, leafy parts of a plant canopy can induce variance in the solid volume fraction, ϕ, across the water depth and thus generate non-uniform drag. Such vertical variation in ϕ could affect the vertical structure of the exchange velocity. Third, our model has only been tested with a narrow range of η. The effects of varying η on the intrusion depth as well as the discharge rate will be a subject of future research. Last, modelling the effects of time-varying radiation intensity, as occurs over the diurnal cycle, was beyond the capabilities of the current experimental configuration. We hope this will be addressed in future field and numerical investigations.

This material is based on work supported by the National Science Foundation under grant EAR0509658. Any opinions, findings or recommendations expressed herein are those of the authors and do not necessarily reflect the views of the National Science Foundation. The authors thank undergraduate student Sebastian Figari for his assistance with the experiments.

REFERENCES

Adams, E. E. & Wells, S. A. 1984 Field measurements on side arms of Lake Anna, VA. *J. Hydraul. Engng* **110** (6), 773–793.

Burke, R. W. & Stolzenbach, K. D. 1983 Free surface flow through salt marsh grass. *MIT Sea Grant Coll. Program Rep.* MITSG 83-16. Massachusetts Institute of Technology.

Chimney, M. J., Wenkert, L. & Pietro, K. C. 2006 Patterns of vertical stratification in a subtropical constructed wetland in south Florida (USA). *Ecol. Engng* **27**, 322–330.

Coates, M. & Ferris, J. 1994 The radiatively driven natural convection beneath a floating plant layer. *Limnol. Oceanogr.* **39** (5), 1186–1194.

Coates, M. J. & Patterson, J. C. 1993 Unsteady natural convection in a cavity with non-uniform absorption of radiation. *J. Fluid Mech.* **256**, 133–161.

Farrow, D. E. 2004 Periodically forced natural convection over slowly varying topography. *J. Fluid Mech.* **508**, 1–21.

Farrow, D. E. & Patterson, J. C. 1993 On the response of a reservoir sidearm to diurnal heating and cooling. *J. Fluid Mech.* **246**, 143–161.

Gharib, M. & Daribi, D. 2000 Digital particle image velocimetry. In *Flow Visualization* (ed. A. J. Smits & T. T. Lim), Chapter 6, pp. 123–147. Imperial College Press.

Horsch, G. M. & Stefan, H. G. 1988 Convective circulation in littoral water due to surface cooling. *Limnol. Oceanogr.* **33** (5), 1068–1083.

Jamali, M., Zhang, X. & Nepf, H. M. 2008 Exchange flow between a canopy and open water. *J. Fluid Mech.* **611**, 237–254.

James, W. F. & Barko, J. W. 1991 Estimation of phosphorus exchange between littoral and pelagic zones during nighttime convection circulation. *Limnol. Oceanogr.* **36** (1), 179–187.

James, W. F., Barko, J. W. & Eakin, H. L. 1994 Convective water exchanges during differential cooling and heating: implications for dissolved constituent transport. *Hydrobiologia* **394**, 167–176.

Kadlec, R. C. 1990 Overland flow in wetlands: vegetation resistance. *J. Hydraul. Engng* **166** (5), 691–706.

Koch, D. L. & Ladd, A. J. C. 1997 Moderate Reynolds number flows through periodic and random arrays of aligned cylinders. *J. Fluid Mech.* **349**, 31–66.

Lei, C. & Patterson, J. C. 2002*a* Natural convection in a reservoir sidearm subject to solar radiation: experimental observations. *Exp. Fluids* **552**, 207–220.

Lei, C. & Patterson, J. C. 2002*b* Unsteady natural convection in a triangular enclosure induced by absorption of radiation. *J. Fluid Mech.* **460**, 181–209.

Lightbody, A., Avener, M. & Nepf, H. M. 2008 Observations of short-circuiting flow paths within a constructed treatment wetland in Augusta, Georgia, USA. *Limnol. Oceanogr.* **53** (3), 1040–1053.

MacIntyre, S. & Melack, J. M. 1995 Vertical and horizontal transport in lakes. Linking moral, benthic, and pelagic habitats. *J. N. Am. Benthol. Soc.* **14**(4), 599–615.

Monismith, S. G., Imberger, J. & Morison, M. L. 1990 Convective motions in the sidearm of a small reservoir. *Limnol. Oceanogr.* **35** (8), 1676–1702.

Oldham, C. E. & Sturman, J. J. 2001 The effect of emergent vegetation on convective flushing in shallow wetlands: scaling and experiment. *Limnol. Oceanogr.* **46** (6), 1486–1493.

Patterson, J. C. 1984 Unsteady natural convection in a cavity with non-uniform absorption of radiation. *J. Fluid Mech.* **140**, 135–151.

Pokorný & Květ 2004 Aquatic plants and lake ecosystems. In *The Lakes Handbook* (ed. P. E. O'Sullivan & C. S. Reynolds), vol. 1, Chapter 11, pp. 309–340. Blackwell Science.

Sturman, J. J. & Ivey, G. N. 1998 Unsteady convective exchange flows in cavities. *J. Fluid Mech.* **386**, 127–153.

Sturman, J. J., Oldham, C. E. & Ivey, G. N. 1999 Steady convective exchange flows down slopes. *Aquat. Sci.* **61**, 260–278.

Sveen, J. K. 2004 An introduction to MatPIV v. 1.6.1. Internet Resources.

Tanino, Y. & Nepf, H. M. 2008 Lateral dispersion in random cylinder arrays at high Reynolds number. *J. Fluid Mech.* **600**, 339–371.

Tanino, Y., Nepf, H. M. & Kulis, P. S. 2004 Gravity currents in aquatic canopies. *Water Resour. Res.* **41** (12), W12402. doi: 10.1029/2005WR004216.

Trevisan, O. V. & Bejan, A. 1986 Convection driven by the non uniform absorption of thermal radiation at the free-surface of a stagnant pool. *Numerical Heat Transfer*, **10**(5), 483–506.

Ultsch, G. 1973 The effect of water hyacinth (Eichhornia crassipes) on the microenvironment of aquatic communities. *Arch. Hydrobiologia* **72**, 460–473.

Wetzel, R. G. 2001 Light in inland water. In *Limnology*, 3rd ed. Academic Press.

Zhang, X. & Nepf, H. M. 2008 Density driven exchange flow between open water and an aquatic canopy. *Water Resour. Res.* **44** (8), W08417. doi: 10.1029/2007WR006676.